A quasar-galaxy merger at $z \sim 6.2$: black hole mass and quasar properties from the NIRSpec spectrum

Federica Loiacono[1], Roberto Decarli[1], Marco Mignoli[1], Emanuele Paolo Farina[2], Eduardo Bañados[3], Sarah Bosman[4,3], Anna-Christina Eilers[5], Jan-Torge Schindler[6], Michael A. Strauss[7], Marianne Vestergaard[8,9], Feige Wang[9], Laura Blecha[10], Chris L. Carilli[11], Andrea Comastri[1], Thomas Connor[12,13], Tiago Costa[14], Massimo Dotti[15,16,17], Xiaohui Fan[9], Roberto Gilli[1], Hyunsung D. Jun[18], Weizhe Liu[9], Alessandro Lupi[15], Madeline A. Marshall[19,20], Chiara Mazzucchelli[21], Romain A. Meyer[22], Marcel Neeleman[23], Roderik Overzier[24], Antonio Pensabene[15], Dominik A. Riechers[25], Benny Trakhtenbrot[26], Maxime Trebitsch[27], Bram Venemans[24], Fabian Walter[3], Jinyi Yang[9]

(Affiliations can be found after the references)

ABSTRACT

We present JWST/NIRSpec integral field data of the quasar PJ308-21 at $z = 6.2342$. As shown by previous ALMA and HST imaging, the quasar has two companion sources, interacting with the quasar host galaxy. The high-resolution G395H/290LP NIRSpec spectrum covers the $2.87 - 5.27$ μm wavelength range and shows the rest-frame optical emission of the quasar with exquisite quality ($S/N \sim 100 - 400$ per spectral element). Based on the Hβ line from the broad line region, we obtain an estimate of the black hole mass $M_{\rm BH,H\beta} \sim 2.7 \times 10^9$ M$_\odot$. This value is within a factor $\lesssim 1.5$ of the Hα-based black hole mass from the same spectrum ($M_{\rm BH,H\alpha} \sim 1.93 \times 10^9$ M$_\odot$) and is consistent with a previous estimate relying on the Mg II λ2799 line ($M_{\rm BH,MgII} \sim 2.65 \times 10^9$ M$_\odot$). All these $M_{\rm BH}$ estimates are within the ~ 0.5 dex intrinsic scatter of the adopted mass calibrations. The high Eddington ratio of PJ308-21 $\lambda_{\rm Edd,H\beta} \sim 0.67$ ($\lambda_{\rm Edd,H\alpha} \sim 0.96$) is in line with the overall quasar population at $z \gtrsim 6$. The relative strengths of the [O III], Fe II and Hβ lines are consistent with the empirical "Eigenvector 1" correlations as observed for low redshift quasars. We find evidence for blueshifted [O III] λ5007 emission with a velocity offset $\Delta v_{\rm [O\,III]} = -1922 \pm 39$ km s^{-1} from the systemic velocity and a FWHM([O III]) = 2776^{+75}_{-74} km s^{-1}. This may be the signature of outflowing gas from the nuclear region, despite the true values of $\Delta v_{\rm [O\,III]}$ and FWHM([O III]) are likely more uncertain due to the blending with Hβ and Fe II lines. Our study demonstrates the unique capabilities of NIRSpec in capturing quasar spectra at cosmic dawn and studying their properties in unprecedented detail.

Key words. quasars: individual: PJ308–21 — quasars: supermassive black holes — galaxies: high-redshift — galaxies: ISM — galaxies: active — ISM: jets and outflows

1. Introduction

High-redshift quasars (or quasi-stellar objects, QSOs) are key laboratories for studying the early stages of galaxy evolution and black hole formation (see Fan et al. 2023 for a recent review). At $z \gtrsim 6$, i.e., when the Universe was $\lesssim 1$ Gyr old, they are often harbored by galaxies with star formation rates SFR $\sim 100 - 4000$ M$_\odot$ yr^{-1}, significantly higher than typical galaxies at similar redshifts with no nuclear activity (e.g., Vanzella et al. 2014; Bouwens et al. 2015; Salmon et al. 2015; Ota et al. 2017; Harikane et al. 2018; Walter et al. 2022). The central black holes can already have masses of 10^9 M$_\odot$ (e.g., Yang et al. 2021; Farina et al. 2022; Mazzucchelli et al. 2023) and the molecular gas content of the host galaxy, which feeds both nuclear and star formation activity, can easily exceed 10^{10} M$_\odot$ (e.g., Walter et al. 2003; Wang et al. 2008; Venemans et al. 2017). Accounting for the rapid growth of $z \gtrsim 6$ quasars poses important challenges to models of early black hole formation and evolution (see, e.g., the reviews by Inayoshi et al. 2020 and Volonteri et al. 2021).

Over the last years, significant effort has been invested to study $z \gtrsim 6$ QSOs using the most advanced facilities. In particular, observations with the *Atacama Large Millimeter/submillimeter Array* (ALMA) and the *Northern Extended Millimeter Array* (NOEMA) have provided a detailed view of

the rest-frame far-infrared emission in these sources. Sub-mm and mm data have enabled deep insights into several properties, such as the gas and dust content (Wang et al. 2008; Calura et al. 2014; Decarli et al. 2018; Venemans et al. 2018; Decarli et al. 2022), kinematics (e.g., Willott et al. 2013, 2015; Venemans et al. 2016; Neeleman et al. 2019; Pensabene et al. 2020; Neeleman et al. 2021) and the physics of the interstellar medium (ISM; Walter et al. 2018; Novak et al. 2019; Li et al. 2020; Pensabene et al. 2021; Meyer et al. 2022b; Shao et al. 2022; Tripodi et al. 2022; Decarli et al. 2023) of quasar host galaxies. Observations at these wavelengths have revealed that $z \gtrsim 6$ QSOs are often associated with companion galaxies from small to large distances, with overdensities exceeding by several orders of magnitude the expectations for the field population of galaxies (Aravena et al. 2016; Decarli et al. 2017; Meyer et al. 2022a; see also Zana et al. 2023 for the theoretical interpretation), even if there are also exceptions to this trend (Mazzucchelli et al. 2017a; Habouzit et al. 2019).

Observations with ground-based optical/near-infrared facilities have constrained the rest-frame ultraviolet (UV) emission from $z \gtrsim 6$ quasars (e.g., Kurk et al. 2007; Willott et al. 2010; Mazzucchelli et al. 2017b; Onoue et al. 2019; Schindler et al. 2020; Yang et al. 2021). For example, integral field data from the Multi Unit Spectroscopic Explorer (MUSE) show that

quasars are often surrounded by Lyman α nebulae extending up to $10 - 30$ kpc (e.g., Borisova et al. 2016; Farina et al. 2017, 2019; Drake et al. 2019). Using X-Shooter detections of the Mg II $\lambda 2799$ and C IV $\lambda 1549$ broad emission lines from quasars, Farina et al. (2022) provided estimates of black hole masses (see also De Rosa et al. 2014; Mazzucchelli et al. 2023), which enabled the study of the scaling relations between black hole and galaxy mass at $z \gtrsim 6$ (e.g., Willott et al. 2017; Izumi et al. 2019; see also Pensabene et al. 2020; Neeleman et al. 2021).

Despite the significant effort with the most advanced ground telescopes that has been invested over the last years, a number of questions remains unsolved. In particular, the rest-frame optical lines from $z > 6$ quasars, shifted to the near- and mid-infrared at those redshifts, represent an uncharted territory due to the limits of the observing facilities in that window.

Now, with the *James Webb Space Telescope* (JWST; Gardner et al. 2023) it is finally possible to study the rest-frame optical emission from $z > 6$ quasars. Observations of emission lines originating from the broad line region (BLR; e.g., Hα and Hβ) provide robust estimates of the black hole mass based on local relations (Greene & Ho 2005; Vestergaard & Peterson 2006; Shen et al. 2011). In addition, the strength and ratios of nebular lines such as Hα, Hβ, [O III] $\lambda\lambda 4959, 5007$, [N II] $\lambda\lambda 6548, 6584$ offer a unique tool to characterize the ISM of the quasar host and companion galaxies, constraining important physical quantities (e.g., the ionization mechanism and the ionization parameter, metallicity, dust extinction), which are not accessible at these redshifts using UV spectra only. First promising results on some of the $z > 6$ quasars observed with JWST come from the "A SPectroscopic survey of biased halos In the Reionization Era" project (ASPIRE; Wang et al. 2023). Based on the ASPIRE data, Yang et al. (2023) studied the rest-frame emission at $4100 - 5100$ Å in a sample of eight $z > 6.5$ quasars while Wang et al. (2023) discovered a filamentary structure tracing an overdensity around a luminous $z \sim 6.6$ QSO (see also Kashino et al. 2023). Marshall et al. (2023) studied two other $z \sim 6.8$ quasars, as well as their host galaxies and companion sources. These works also provide first estimates of black hole masses at $z > 6$ measured with the Hβ or Hα line (see also Bosman et al. 2023; Ding et al. 2023; Eilers et al. 2023; Yue et al. 2023).

PJ308-21 at $z = 6.2342$ stands out among the known quasars at $z > 6$ as a key laboratory to study quasar-galaxy interactions at cosmic dawn. This object was discovered by Bañados et al. (2016) (see also Mazzucchelli et al. 2017b) and intensively studied by Decarli et al. (2019) using high-resolution ALMA data, targeting the [C II] and dust continuum emission in this system. The ALMA observations reveal that the quasar host has two companion sources, respectively blueshifted ($\Delta v_{\rm [CII]} \sim -750$ km s^{-1}; Decarli et al. 2019) and redshifted ($\Delta v_{\rm [CII]} \sim +500$ km s^{-1}) from the quasar, located toward the western and eastern sides of the quasar at projected distances of ~ 5 and $\gtrsim 10$ kpc respectively. These two emission components are also detected in rest-frame UV images from the *Hubble Space Telescope* (HST), revealing light from young stars from both objects. As discussed by Decarli et al. (2019), the quasar host is possibly experiencing a merger with another galaxy, tidally disturbed by the interaction and which accounts for the emission from the two companion sources. Deep MUSE observations reveal that the system is surrounded by a Lyman α halo ($R \sim 27$ kpc), which overlaps with the eastern companion (Farina et al. 2019). Furthermore, Connor et al. (2019) found that PJ308-21 has an X-rays luminosity $L_X(2 - 10 \text{ keV}) \sim 2 \times 10^{45}$ erg s^{-1} while the western companion shows possible high-energy emission with no soft component, which may point to an AGN nature also for this object. Because

of its complex and extended morphology, the PJ308-21 system is an ideal target for JWST/NIRSpec integral field spectroscopy, which allow us to probe rest-frame optical emission of the spatially resolved components of this object.

This work (Paper I) is the first of a series of papers studying the PJ308-21 system with NIRSpec data. In particular, it is devoted to the characterization of the quasar spectrum itself. Paper II (Decarli et al., in prep.) studies the extended gas emission in the system. Paper III (Farina et al. in prep.) investigates the Lyman α/Hα halo. Yet another paper will focus on the kinematics of the system.

This paper is organized as follows. Sect. 2 deals with the NIRSpec observation and data reduction. Sect. 3 is devoted to the analysis of the QSO spectrum. In Sect. 4 we present the results of our analysis. Finally, we summarize our conclusions in Sect. 5.

In this work we adopt a ΛCDM cosmology with $\Omega_\Lambda = 0.7$, $\Omega_M = 0.3$ and a Hubble constant $H_0 = 70$ km s^{-1} Mpc^{-1}.

2. Observations and data reduction

In this paper we analyze the data of the Cycle 1 General Observers (GO) program 1554 (PI: R. Decarli) that targets the PJ308-21 quasar system (see Table 1 of Decarli et al. 2019 for the properties of the system derived from ALMA and HST data). The observations were taken on September 22-23 2022 using the integral field unit (IFU) of JWST/NIRSpec (Jakobsen et al. 2022; Böker et al. 2022). The science observations consist of two separated fields ($3'' \times 3''$ each), corresponding to the quasar and its western companion (PJ308-W), and to the eastern component (PJ308-E) respectively. A third field covered an empty region of the sky to estimate the background. We observed each field (background included) for 2 hours and 30 minutes (including overheads), for a total execution time of 7.5 hours (4.8 hrs on source). We used the NRSIRS2 readout in order to minimize the correlated noise and the data volume, and observed a total of 18 exposures (6 per pointing applying a small-cycling dithering pattern), each of them consisting of 13 groups (i.e., integration elements). We also observed one leakage exposure of 87 seconds to remove the pattern introduced by the NIRSpec Micro-Shutter Array (MSA).

The data were taken in the high-resolution mode (spectral power $R \sim 2700$) using the G395H/290LP grating-filter combination. This covers the wavelength range $2.87 - 5.27$ μm with a gap due to the NRS1 and NRS2 detector separation corresponding to $4.1 - 4.3$ μm .

We reduced the data using the JWST pipeline developed by the Space Telescope Science Institute (STScI). We use the 1.12.5 version of the pipeline combined with the Calibration Reference Data System (CRDS) context `jwst_1183.pmap`, which indicates the set of reference files necessary for calibrating the data. The reduction process consists of three stages, each of them involving several steps (see Figure 1). Stage 1 processes the raw exposures (i.e., non-destructive readout ramps) correcting for detector effects like bias, dark and cosmic rays impact, and creates count rate images. During this stage, we introduce a further flagging of the ramps strongly affected by saturation, non-linearity or cosmic rays (`Further ramp flagging` in Figure 1). In particular, we exclude from the ramp fitting all the ramps containing only two useful groups (out of 13). This step results in a drop of the standard deviation in the rate files (i.e., 2D count-rate images) by a factor $\lesssim 2 \times 10^3$. The rate files are affected by vertical stripes due to residual $1/f$ noise unremoved in stage 1 (see also Kashino et al. 2023; Perna et al. 2023; Rauscher 2023).
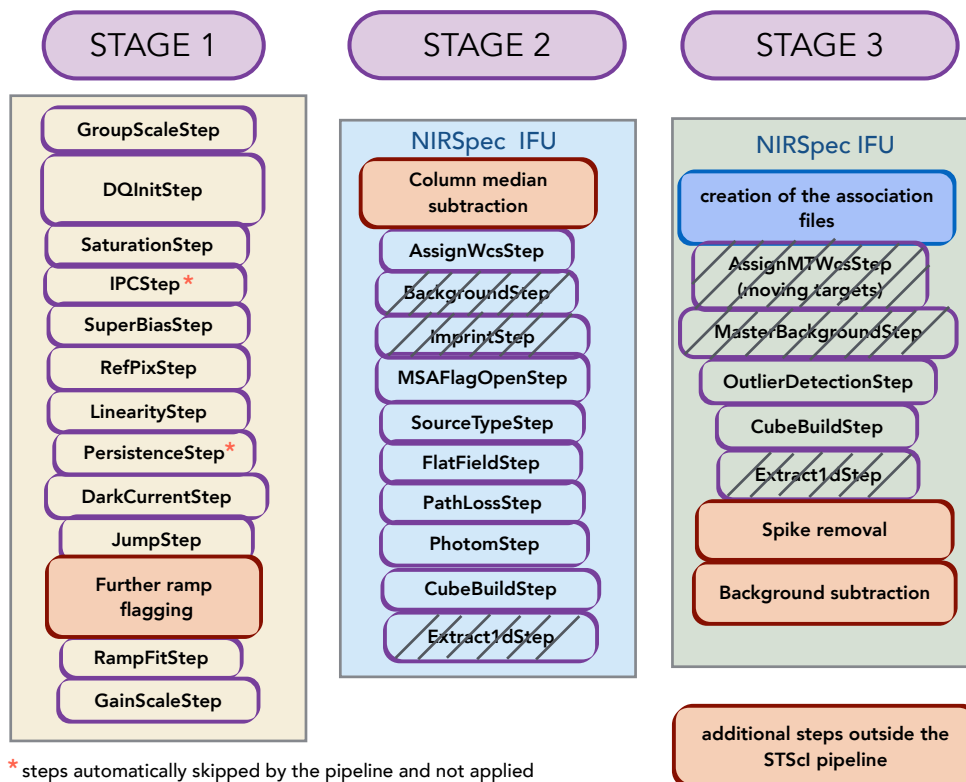
Fig. 1. Scheme of the data reduction process for the NIRSpec data of PJ308-21. The data reduction is divided into three stages, each of them consisting of several steps. Stage 1 is independent from the JWST instrument and mode, unlike stage 2 and 3, for which we present the steps for NIRSpec/IFU. We skip some pipeline steps (boxes with grey tilted lines) and introduce additional steps (orange boxes) to improve the data reduction (see Section 2).

We eliminate this pattern by subtracting from each spectral column in the 2D count-rate images its median value, which provides a reasonable estimate of any spectrally-dependent correlated noise (see `Column median subtraction` in Figure 1).

We thus process the median-subtracted exposures through stage 2 of the reduction, where flat field correction, wavelength and flux calibration are applied to all the exposures. We skip the `BackgroundStep`, as we apply the background subtraction at the end of stage 3. We also skip the `ImprintStep`, which is meant to subtract the pattern created by the MSA, as we found that the subtraction of a dedicated leakage exposure results in a detrimental increase of the noise in the rate files.

We then perform stage 3, where all the exposures are combined into the final datacubes. We apply the `OutlierDetectionStep`, which is meant to remove the remaining bad pixels from the calibrated exposures, and which provides reliable results for our dataset from the 1.11.4 pipeline version.

The one-dimensional spectra extracted from random apertures in the final datacubes show several spikes, due to cosmic rays and possible wrong solutions for the ramp fitting. We filter out these spikes by masking all the voxels that present a jump between contiguous channels persisting for less than four channels (corresponding to < 150 km s^{-1} at 4.0 μm), which is the typical width of the spikes. The procedure is applied to all the voxels of the datacubes (see `Spike removal` in Figure 1). We carefully inspect the voxels corresponding to the science targets before/after applying this step to check that none of the emis-

sion lines is affected by the algorithm. Finally, we subtract the background, which is higher for the spectral region sampled by the NRS2 detector ($4.3 - 5.3$ μm), as the NIR background grows with increasing wavelength (Rigby et al. 2022). We estimate the background from the median of spectra extracted from empty regions in the FOV as a function of wavelength. The median background is then subtracted from the datacubes channel-by-channel (see `Background subtraction` in Figure 1).

In this paper, as we are interested in the quasar spectrum, we study the PJ308-W pointing only. A map showing an overlook on the system captured by the PJ308-W and PJ308-E reduced datacubes is shown in Figure 2 (see Decarli et al., in prep., for more details).

3. Analysis

3.1. Spectrum extraction and aperture correction

We compute a wavelength-dependent aperture correction based on the observation of a point source (i.e., a star) using archival data. We use the uncalibrated exposures of the GSPC P330-E G–dwarf, observed in the 1538 calibration program (PI: K. Gordon). We opt for this star as it was observed with NIRSpec/IFU using the same grating/filter combination of our observation. We process the data, applying the same steps described in Sect. 2. The final datacube is used for extracting one-dimensional spectra adopting circular apertures with radii R ranging from $R = 0.025''$ to $R = 1.2''$ centered on the star. The growth curve asymptotes at $1''$, so we normalize the flux in each wavelength channel to the
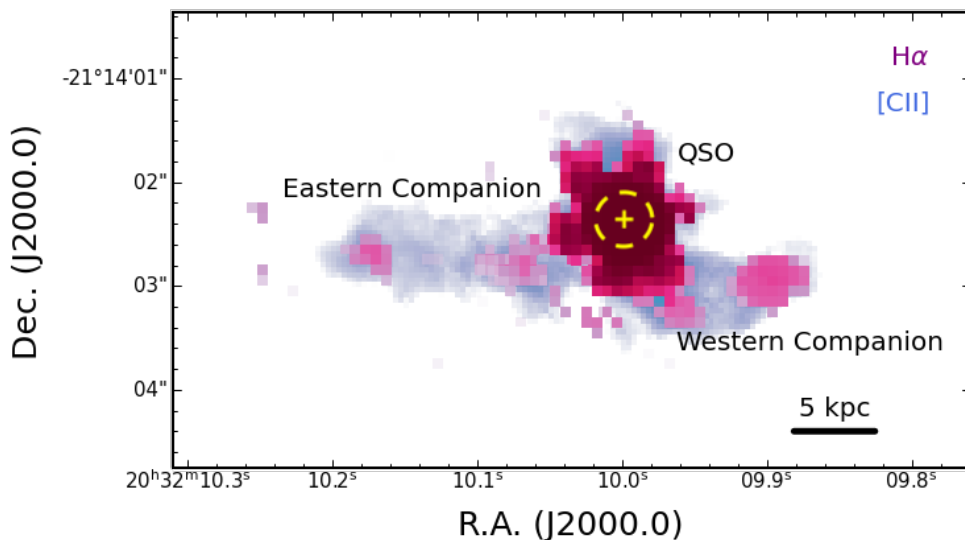
Fig. 2. The PJ308-21 system. The quasar has two companion sources, located to the western and eastern sides of the QSO respectively. We show the Hα and the underlying continuum emission from the NIRSpec/IFU data (magenta) overimposed on the [C II] emission from ALMA high-resolution data (blue; Decarli et al. 2019). The yellow cross and circle show the aperture for the spectrum extraction (see Sect. 3.1).

value at $R = 1''$ (see also Fig A.1 in Appendix A). We thus estimate the flux fraction for fixed aperture radii as a function of the wavelength (see Table 1 for representative wavelengths over the G395H/F290LP spectral range). We compute these values by fitting a second–order spline to the flux fractions. The enclosed flux fraction increases with increasing radius and, for fixed aperture, decreases with wavelength. The latter trend is less pronounced at larger radii, as most of the flux is also included for the redder part of the spectrum (see also Fig A.1 in Appendix A). For an aperture of $0.3''$, the flux loss between the red and blue channels can be as high as ∼ 6%, while the difference is lower for larger apertures.

The values reported in Table 1 can be used to correct the spectra extracted from apertures with radii $R \sim 0.3'' - 0.7''$ to recover the total flux emitted by a point source. These values should provide reliable corrections when using the dataset observed using the NIRSpec/IFU with the G395H/F290LP grating/filter combination and the adopted version of the pipeline[1]. We adopt an extraction aperture of $0.3''$ centered at the NIRSpec peak position of PJ308-21 (Figure 2). We note that using a larger aperture, i.e., $0.4'' - 0.7''$, after applying the aperture correction gives perfectly consistent results, while using a smaller aperture (∼ $0.2''$) cannot properly recover the QSO flux because of the undersampling of NIRSpec PSF (see Böker et al. 2022). We thus apply the $0.3''$ aperture correction based on Table 1 to recover the total flux. The same correction is applied to the error spectrum. We obtain the noise spectrum by summing all the pixel variance over the $0.3''$ aperture and extracting the square root of the summed total. We show in Fig. 3 the aperture-corrected spectrum together with the rest-frame UV spectra of PJ308-21 from the literature, obtained with MUSE (Farina et al. 2019) and XSHOOTER (Schindler et al. 2020). The S/N of the NIRSpec spectrum per spectral element is $100 - 400$. We show also the photometric data (see Bañados et al. 2016) from the first release

of the Panoramic Survey Telescope and Rapid Response System (Pan-STARRS1, PS1; *g, r, i, z, Y* bands), the Gamma-ray Burst Optical/Near-infrared Detector (GROND; *i, z, J* bands), the VISTA Hemisphere Survey (VHS; *Y, H, K* bands), *Spitzer (Ch1=3.5 μm, Ch2=4.5 μm)* and the Wide-Field Infrared Survey Explorer (WISE; *W1*=3.3 μm, *W2*=4.6 μm). There is an overall agreement between the NIRSpec spectrum and the available photometry from *Spitzer* and WISE. The differences, in the order of ∼ 10%, are possibly due to systematics in the instruments zero-points. We note that the continuum slope changes between the NIRSpec data and the ground-based spectra. This is possibly due to both physical and instrumental effects. The power-law continuum in quasars is interpreted as the result of several black bodies, corresponding to layers in the accretion disk with different temperatures. The large black hole mass (see Sect. 4.1) yields a relatively large radius of the innermost ring, which corresponds to a peak in the continuum emission. Therefore, the quasar continuum is expected to change the slope from the rest-frame UV (where most of the disk emission is expected) to rest-frame optical. Second, the fluxes in the XSHOOTER spectrum are expected to be more extinguished from the dust in the quasar host in comparison to the near-infrared data, which can also influence the slope. Beyond these physical effects, possible systematics in the zero-points, potential slit losses in the XSHOOTER spectrum, uncertainties in the NIRSpec flux calibration and increased noise toward the red end of the XSHOOTER spectrum can also contribute to the slope variation.

3.2. Spectral fitting

We convert the observed wavelength into the rest-frame using the [C II] based redshift ($z = 6.2342$, Decarli et al. 2019). The spectrum shows a strong quasar continuum and all the prominent Balmer lines (Hα, Hβ, Hγ, Hδ) due to the BLR. We also observe bright emission from the Fe II multiplets in the $4000 - 5500$ Å range. The BLR dominates over the nebular emission of the narrow line region (NLR; i.e., [O III] $\lambda\lambda4959, 5007$ and [N II] $\lambda\lambda6548, 6584$ doublets). We do not detect a significant He II $\lambda4686$ emission line, which can be used as a tracer of the nuclear
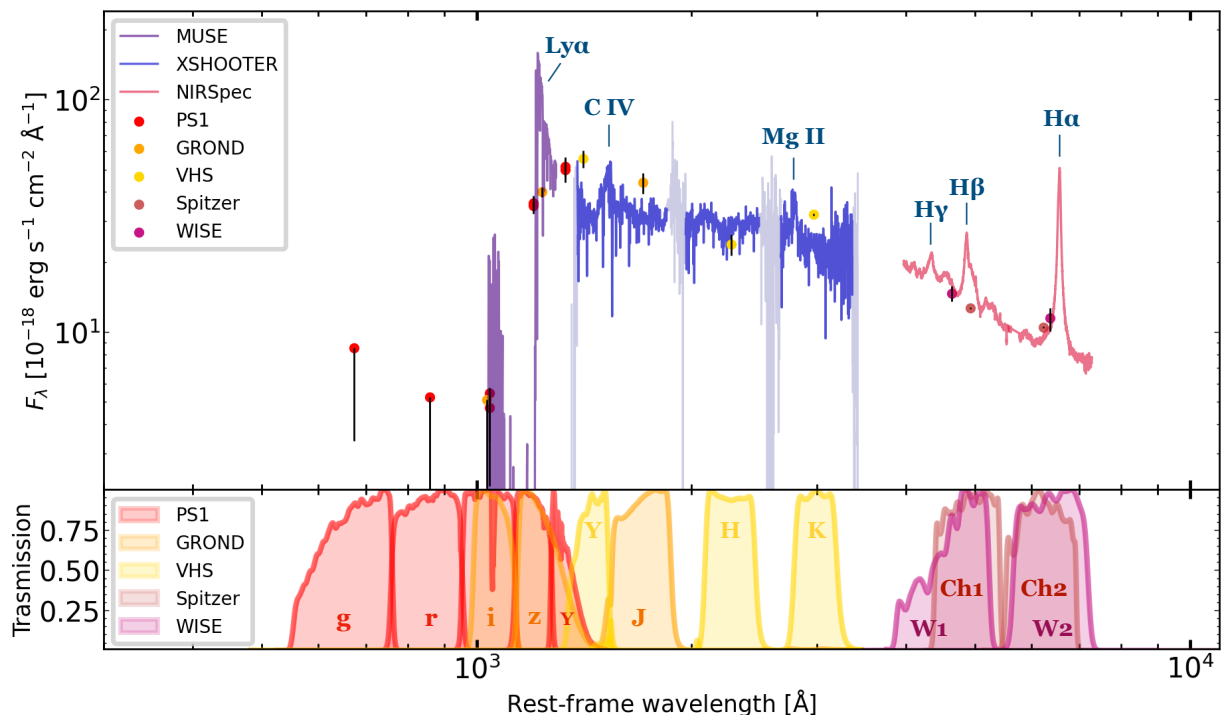
---

[1] We also test the procedure on another unresolved source, IRAS 05248-7007, observed with the G395H/F290LP grating/filter setup in the NIRSpec calibration program 1492 (PI: T. Beck). For apertures of $0.3'' - 0.7''$ we obtain flux fractions that differ from the values reported in Table 1 by less than 1%.

Fig. 3. Rest-frame UV/optical spectroscopic and photometric data of PJ308-21. The main emission lines are indicated. The aperture-corrected NIRSpec spectrum is shown in red. The purple and blue lines show MUSE and XSHOOTER spectra from previous works (Farina et al. 2019; Schindler et al. 2020). We show in grey the XSHOOTER data affected by the atmosphere absorption. The photometric data from Pan-STARRS1 (PS1; *g, r, i, z, Y* bands), GROND (*i, z, J* bands), VHS (*Y, H, K* bands), *Spitzer* (*Ch1*=3.5 μm, *Ch2*=4.5 μm) and WISE (*W1*=3.3 μm, *W2*=4.6 μm) are shown with the associated errors (Bañados et al. 2016).

Table 1. Flux fraction for fixed aperture radius R as a function of the wavelength (NIRSpec/IFU, G395H/F290LP).

Wavelength (μm)	0.3″	0.4″	0.5″	0.6″	0.7″
2.90	0.891	0.926	0.953	0.964	0.973
3.00	0.891	0.926	0.952	0.964	0.974
3.20	0.890	0.925	0.950	0.965	0.976
3.40	0.888	0.924	0.948	0.966	0.977
3.60	0.885	0.923	0.947	0.966	0.977
3.80	0.882	0.922	0.945	0.966	0.978
4.00	0.877	0.921	0.944	0.965	0.978
4.20	0.872	0.920	0.942	0.963	0.978
4.40	0.866	0.919	0.941	0.962	0.977
4.60	0.859	0.918	0.940	0.959	0.976
4.80	0.852	0.916	0.938	0.957	0.975
5.00	0.843	0.915	0.937	0.954	0.973
5.10	0.839	0.914	0.936	0.952	0.973
5.20	0.834	0.914	0.936	0.950	0.972

activity (Tozzi et al. 2023), or significant [S II] $\lambda\lambda 6716, 6732$ emission. Also, we do not find absorption features over the NIRSpec spectrum.

3.2.1. Continuum subtraction

We perform a multicomponent fitting to reproduce the NIRSpec spectrum using a Markov chain Monte Carlo (MCMC) method with the Python package `emcee` (Foreman-Mackey et al. 2013). We first model the continuum emission, whereafter we model the iron and the nebular lines.

Quasar spectra often show a break in their shape, possibly

due to the host galaxy contamination (see, for example, Vanden Berk et al. 2001). For this reason, we use a broken power-law to model the continuum emission, in the functional form of

$$f(\lambda) = \begin{cases} A\left(\dfrac{\lambda}{\lambda_{\text{break}}}\right)^{-\alpha_1} & : \lambda < \lambda_{\text{break}} \\ A\left(\dfrac{\lambda}{\lambda_{\text{break}}}\right)^{-\alpha_2} & : \lambda \geq \lambda_{\text{break}} \end{cases}$$

where A is the normalization, λ_{break} is the break wavelength and α_1 and α_2 are the power-law indices. Following Vanden Berk et al. (2001), we use the line-free regions of the spectra $6005 - 6035$ Å and $7160 - 7180$ Å with an additional region at $4000 - 4030$ Å to constrain the bluest part of the spectrum, after carefully checking that it is not contaminated by line emission (see the shaded regions in Figure 4, top panel) to fit the continuum. The continuum model is shown in Figure 4 (top panel), with the continuum-subtracted spectrum highlighted in orange (see also Table 2 for the fitted parameters). We do not discuss the physical meaning of the λ_{break}, A, α_1 and α_2 values and compare with low-redshift quasars, as we find that the parameters are highly degenerate among themselves. We thus use the fit only to obtain a robust continuum-free spectrum for fitting the emission lines.

3.2.2. Fe II subtraction

After subtracting the continuum, we model the Fe II multiplets in the spectral range $4000 - 5500$ Å. Careful subtraction of the Fe II emission is indeed necessary for deriving an accurate Hβ-based black hole mass (see Sect. 4.1), as this line is partially

Table 2. Continuum and iron fitted parameters.

Parameter	Value
A^+	$10.28^{+1.29}_{-2.21}$
$\lambda_{\text{break}}/\text{Å}$	$5330.65^{+1059.70}_{-542.29}$
α_1	$2.16^{+0.65}_{-0.32}$
α_2	$1.08^{+0.04}_{-0.37}$
I^+_{ZwI}	$1.28^{+0.03}_{-0.03}$
I^+_{S}	$1.16^{+0.03}_{-0.03}$
I^+_{F}	$0.72^{+0.01}_{-0.01}$
I^+_{P}	$0.59^{+0.05}_{-0.05}$
I^+_{G}	$0.90^{+0.01}_{-0.01}$

Notes. The errors correspond to the 16th and 84th percentiles of the MCMC fit. $^{(+)}$The normalization units are 10^{-18} erg s^{-1}cm^{-2}Å^{-1}.

contaminated by iron emission. We use the tool by Kovačević et al. (2010) and Shapovalova et al. (2012) to create an Fe II template consisting of five groups of lines (labeled as Zw I, S, F, P, G), using reasonable input parameters for an AGN spectrum (i.e. temperature $T = 10000\,K$, velocity width of 2500 km s^{-1} and no velocity shift). However, using a different set of input parameters does not change the fit results significantly. In particular, we verify that increasing the Fe II width, by smoothing it to match the width of other BLR lines, does not significantly impact the black hole mass derived from the broad Hβ full-width at half-maximum (FWHM; see Sect 4.1). We fit the normalization of the five groups (labeled as I_{ZwI}, I_{S}, I_{F}, I_{P}, I_{G}, see Table 2) to properly rescale the templates using the spectral regions at $4150 - 4200$ Å, $4430 - 4720$ Å and $5110 - 5520$ Å (shaded regions in Figure 4, bottom panel). The Fe II model is shown in Figure 4 (bottom panel), with the iron-subtracted spectrum in orange (see also Table 2 for the fitted parameters). We use the templates of Kovačević et al. (2010) and Shapovalova et al. (2012), which secure reliable multiplets structure and intensity. However, the high S/N of our spectrum highlights the limits of the models. Introducing variable widths among the templates due to a velocity stratification of the BLR could possibly improve the fit compared to the simple case here presented.

3.2.3. Line fitting

After subtracting the continuum and Fe II model, we fit the line emission. In particular, we focus on the Hα and Hβ line complexes, since we use these lines to derive relevant physical quantities (e.g., black hole mass; see Sect. 4). We use two Lorentzian functions (one for each line) to model the Hα and Hβ lines from the BLR (Kollatschny & Zetzl 2013), leaving all parameters (i.e., normalization, width and centroid) free. We also insert six Gaussians to account for the nebular [O III] $\lambda\lambda 4959, 5007$, [N II] $\lambda\lambda 6548, 6584$, H$\alpha$ and Hβ lines from the NLR (referred to as "narrow" components in the rest of the text). As the emission is completely dominated by the broad Hα and Hβ lines, we fix the line centroids to the theoretical values to aid the fit, by assuming that the rest-frame velocity of the narrow lines is consistent with the [C II] velocity. We also require that all six narrow lines have the same velocity width and fix the ratio of the amplitudes of [O III] $\lambda 4959$ and [O III] $\lambda 5007$ to the theoretical value (0.33), as well as for the [N II] $\lambda 6548$ and [N II] $\lambda 6584$ (0.33; e.g., Osterbrock & Ferland 2006). Thus, for the NLR lines, we fit only the

normalization of [O III] $\lambda 5007$, [N II] $\lambda 6584$, Hα, Hβ and the standard deviation (σ). Moreover, we add two further Gaussian components to reproduce the emission at $4900 - 5100$ Å (the "broad" [O III] components discussed in Sect 4.4). Under the assumption that this emission is due to [O III] $\lambda\lambda 4959, 5007$ blueshifted with respect to the systemic velocity, we require that the two Gaussians have the same velocity width and offset, and the theoretical ratio for the amplitudes. Therefore, in this case, the free parameters are the centroid, σ and the normalization of the [O III] $\lambda 5007$ component.

We adopt Maxwellian priors for all the fitted parameters except for the width of the narrow components. In this case we impose that the FWHM can uniformly vary between 50 and 1000 km s^{-1} (a similar approach was adopted by Vietri et al. 2018). The fitted wavelength ranges are $4430 - 5520$ Å and $6160 - 6900$ Å. The fit is shown in Fig. 5 (see also Table 3).

Our multicomponent fit nicely reproduces the line emission for both Hα and Hβ regions. As seen for the continuum fitting, the galactic contribution (i.e., NLR emission) is poorly constrained, as the BLR dominates the line emission. There are some residuals at $5000 - 5200$ Å, possibly due to uncertainties in the iron modeling described in Sect. 3.2.2. However, this does not significantly impact the Hβ fit and the Hβ-based black hole mass estimates. Finally, we note that using a broken power-law rather than a Lorentzian curve to model the Hα and Hβ lines from the BLR also gives a consistent black hole mass. The BLR emission may have indeed asymmetric wings that are better reproduced by a broken power-law. A study of these features is however beyond the scope of this work. We also test that adding a broad component for the Hα and Hβ lines, as done for the [O III] emission, does not affect the fit, as both the components are in the order of the residuals.

4. Results

4.1. Black hole mass

A common way to estimate the black hole mass in quasars relies on the virial theorem. Assuming that the clouds of the BLR undergo pure gravitational motion around the black hole, we can write the black hole mass as $M_{\text{BH}} = R_{\text{BLR}} v^2_{\text{BLR}}/G$, where G is the gravitational constant, v_{BLR} the clouds' velocity and R_{BLR} their distance from the black hole. Based on reverberation mapping studies in the low-z Universe, the continuum luminosity at 5100 Å is correlated with R_{BLR} (e.g., Kaspi et al. 2005), while the FWHM of the BLR lines (e.g., Hβ, Hα, Mg II, C IV) provide the information for the velocity v_{BLR}. Before the JWST launch, emission lines such as Mg II and, more rarely, C IV were commonly used to measure the black hole masses in high-z quasars (e.g., Jun et al. 2015; Lira et al. 2018; Onoue et al. 2019; Kaspi et al. 2021; Farina et al. 2022). However, the relations that employ these tracers are actually poorly constrained and uncertain, especially for the C IV line (Coatman et al. 2017; Marziani et al. 2019; Homayouni et al. 2020; Zuo et al. 2020). It is thus not clear if the black hole masses based on these lines are reliable. On the other hand, Hβ has been extensively studied to derive empirical calibrations for black hole mass at low redshift (e.g., Bentz et al. 2009; De Rosa et al. 2018; see Shen 2013 for a review), and it is thus considered the most robust tracer of this physical quantity. After the launch of JWST, we can now use this line for measuring the black hole mass even at high-redshift (see also Ding et al. 2023; Eilers et al. 2023; Marshall et al. 2023; Yang et al. 2023).

We estimate the black hole mass of PJ308-21 using the relation of Vestergaard & Peterson (2006), which uses the 5100 Å
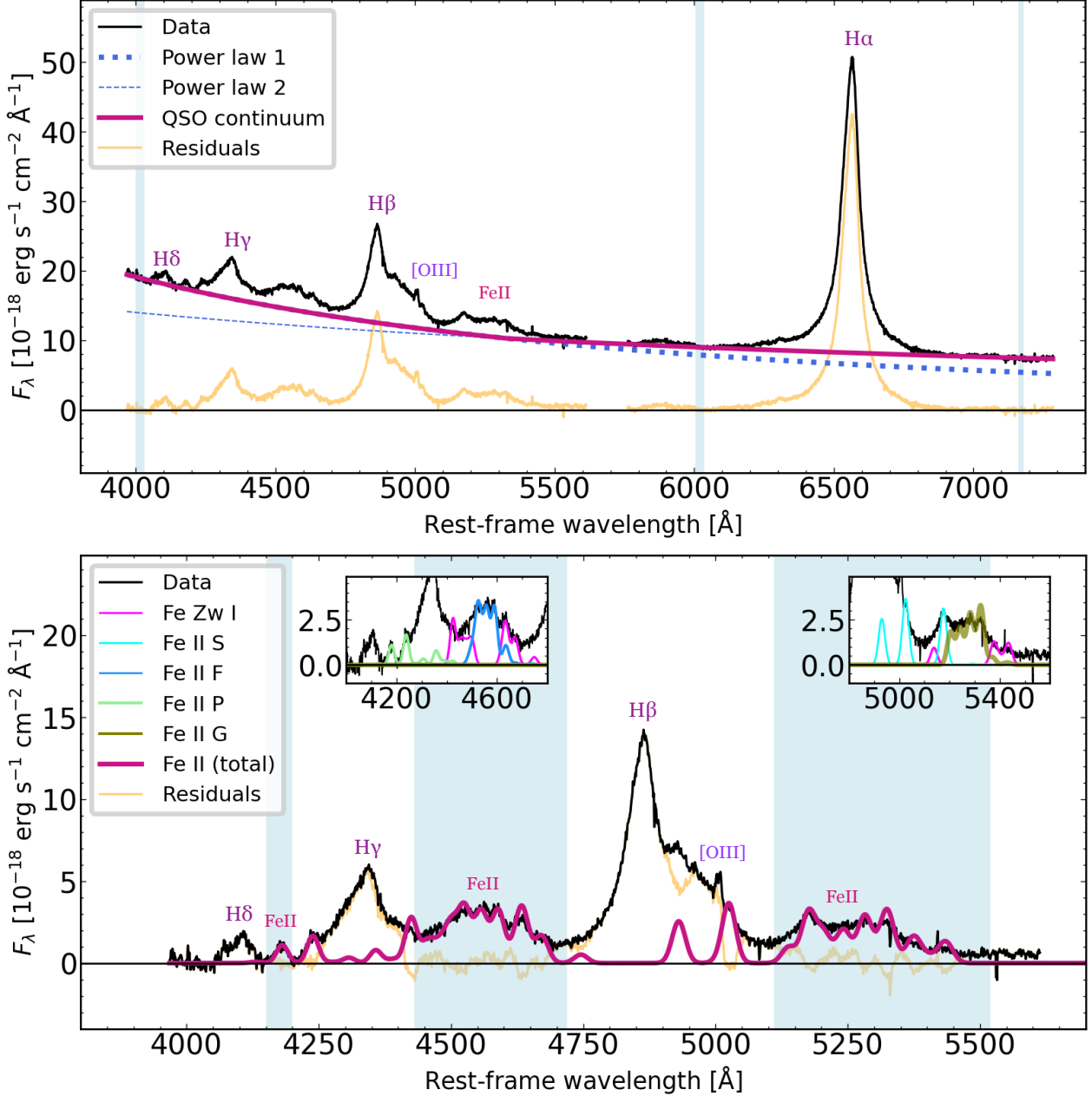
Fig. 4. JWST/NIRSpec rest-frame optical spectrum of the PJ308-21 quasar (black). The spectrum was extracted from a 0.3″ aperture and then aperture corrected to account for the PSF broadening with wavelength (see Sect. 3.1). Broad Balmer line emission (Hα, Hβ, Hγ, Hδ), strong Fe ɪɪ and [O ɪɪɪ] emission is clearly seen. *Top panel:* QSO continuum fit (magenta curve). We highlight the line-free regions used for the continuum fit (pale blue). The orange curve shows the residuals. *Bottom panel:* Fe ɪɪ line model (magenta). The fitted wavelengths are highlighted in pale blue. We fit the Fe ɪɪ emission using the five multiplets template of Kovačević et al. (2010) and Shapovalova et al. (2012) (colored lines in the insets). The iron-subtracted spectrum (orange) was then used to fit the Balmer and nebular lines.

QSO continuum luminosity $L_\lambda(5100 \text{ Å})$ and the FWHM of the Hβ:

$$\log\left(\frac{M_{\mathrm{BH,H\beta}}}{M_\odot}\right) = 2\log\left(\frac{\mathrm{FWHM(H\beta)}}{1000 \text{ km s}^{-1}}\right) + 0.5\log\left(\frac{\lambda L_\lambda(5100\text{Å})}{10^{44}\text{erg s}^{-1}}\right) + 6.91 \tag{1}$$

We estimate the continuum monochromatic luminosity $L_\lambda(5100 \text{ Å}) = (4.9^{+0.4}_{-0.2}) \times 10^{42} \text{ erg s}^{-1}\text{Å}^{-1}$ from the power law value at 5100 Å while the FWHM(Hβ) is $4616^{+63}_{-61} \text{ km s}^{-1}$. The

black hole mass is:

$$M_{\mathrm{BH,H\beta}} = (2.7 \pm 0.2) \times 10^9 \text{ M}_\odot$$

We note that the uncertainties on the black hole mass due to random errors from the MCMC fit are around the 7%. However, the adopted calibration has an intrinsic scatter of ∼ 0.5 dex, which thus represents the main source of uncertainty (Vestergaard & Peterson 2006).

Greene & Ho (2005) found that there is a correlation between the 5100 Å continuum luminosity and the Hα luminosity (see their Eq. 1). A correlation is also present between the Hβ and
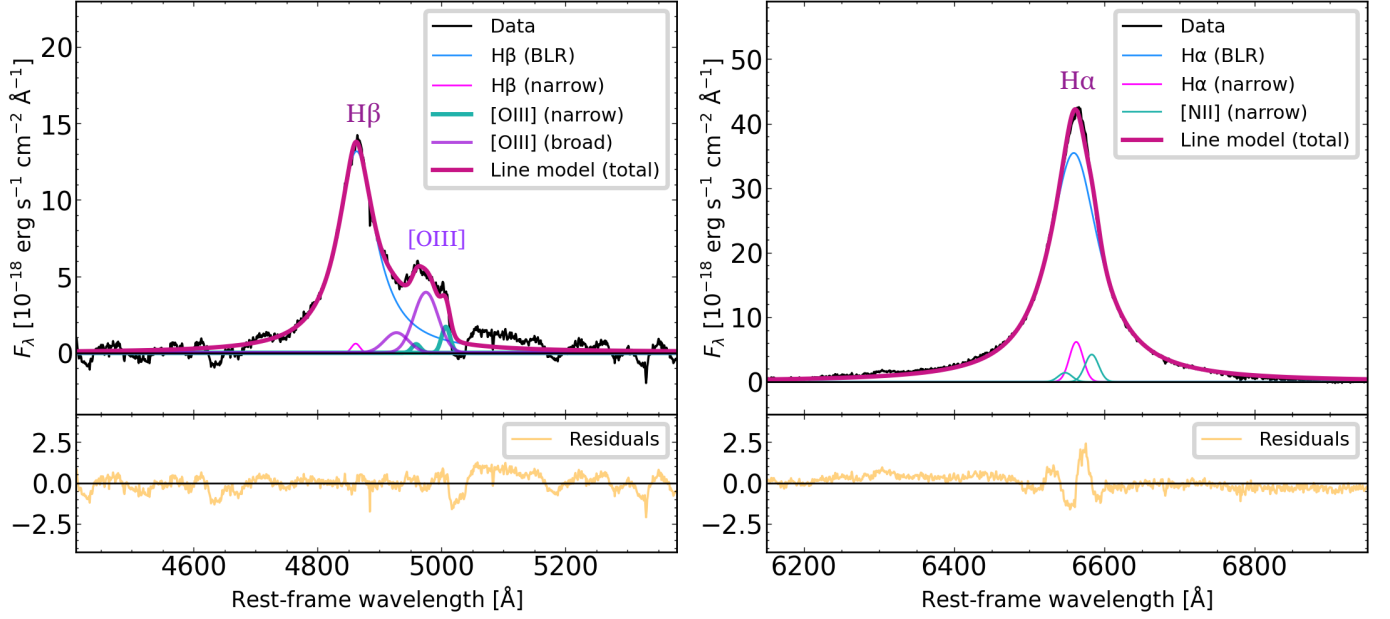
Fig. 5. Fit of the Hβ + [O III] (*left*) and Hα + [N II] lines (*right*), after the continuum and iron subtraction. We model the BLR Hβ and Hα lines using a Lorentzian function. The nebular lines from the NLR ([O III], [N II], Hα, Hβ narrow components) are each fitted with a Gaussian. We add two further Gaussian components (purple; "broad" components in the text) to fit the emission around 5000 Å, likely associated with blueshifted [O III] (see also Sect. 4.4 and Figure 8). The residuals are shown in orange.

Table 3. Emission-line fitted parameters.

Line	Centroid (Å, rest-frame)	σ (Å, rest-frame)	Peak flux (10^{-18} erg s^{-1}cm^{-2}Å^{-1})
Hα (BLR)	$6559.53^{+0.16}_{-0.15}$	$40.91^{+0.28}_{-0.28}$ *	$35.46^{+0.31}_{-0.31}$
Hβ (BLR)	$4862.76^{+0.25}_{-0.24}$	$37.43^{+0.51}_{-0.50}$ *	$13.18^{+0.14}_{-0.14}$
Hα (NLR)	_	tied	$15.41^{+0.80}_{-0.81}$
Hβ (NLR)	_	tied	$1.52^{+0.52}_{-0.51}$
[N II] $\lambda6548$ (NLR)	_	tied	tied
[N II] $\lambda6584$ (NLR)	_	tied	$10.60^{+0.65}_{-0.66}$
[O III] $\lambda4959$ (NLR)	_	tied	tied
[O III] $\lambda5007$ (NLR)	_	$6.98^{+0.02}_{-0.04}$	$4.27^{+0.38}_{-0.38}$
[O III] $\lambda4959$ (broad)	tied	tied	tied
[O III] $\lambda5007$ (broad)	$4974.74^{+0.65}_{-0.64}$	$19.60^{+0.53}_{-0.52}$	$9.93^{+0.23}_{-0.23}$

Notes. The errors correspond to the 16th and 84th percentiles of the MCMC fit. A "_" indicates the fixed parameters. (*) The reported σ is the half-width at half maximum of a Lorentzian function in the functional form $f(\lambda) = f_{\rm peak}\sigma^2/[(\lambda - \lambda_{\rm peak})^2 + \sigma^2]$, where $f_{\rm peak}$ and $\lambda_{\rm peak}$ are the peak flux and centroid respectively.

Hα FWHM (see their Eq. 3; see also Shen et al. 2011, Eq. 9). Using these correlations and Eq. 1 it is thus possible to obtain a calibration for the black hole mass with the Hα line (Shen et al. 2011):

$$\log\left(\frac{M_{\rm BH,H\alpha}}{M_\odot}\right) = 0.379 + 0.43\log\left(\frac{L(H\alpha)}{10^{42}\,{\rm erg\,s^{-1}}}\right) + 2.1\log\left(\frac{{\rm FWHM}(H\alpha)}{{\rm km\,s^{-1}}}\right) \tag{2}$$

where $L(H\alpha)$ and FWHM(Hα) are the luminosity and FWHM of the Hα broad component. We estimate the former quantity $L(H\alpha) = (1.84 \pm 0.01) \times 10^{45}$ erg s^{-1} by integrating the Hα Lorentzian component from 6300 Å to 6800 Å. The FWHM of

the Lorentzian is FWHM(Hα) = 3739 ± 26 km s^{-1}. The resulting Hα-based black hole mass is

$$M_{\rm BH,H\alpha} = (1.93 \pm 0.03) \times 10^9\,M_\odot$$

We find that the $M_{\rm BH,H\beta}$ and $M_{\rm BH,H\alpha}$ values agree with each other within a factor of $\lesssim 1.5$ (see also Table 4), as expected from the intrinsic scatter of the adopted correlations.

We can compare our estimates of the black hole mass with the Mg II-based measurement for PJ308-21. Based on the relation of Shen et al. (2011), Farina et al. (2022) found

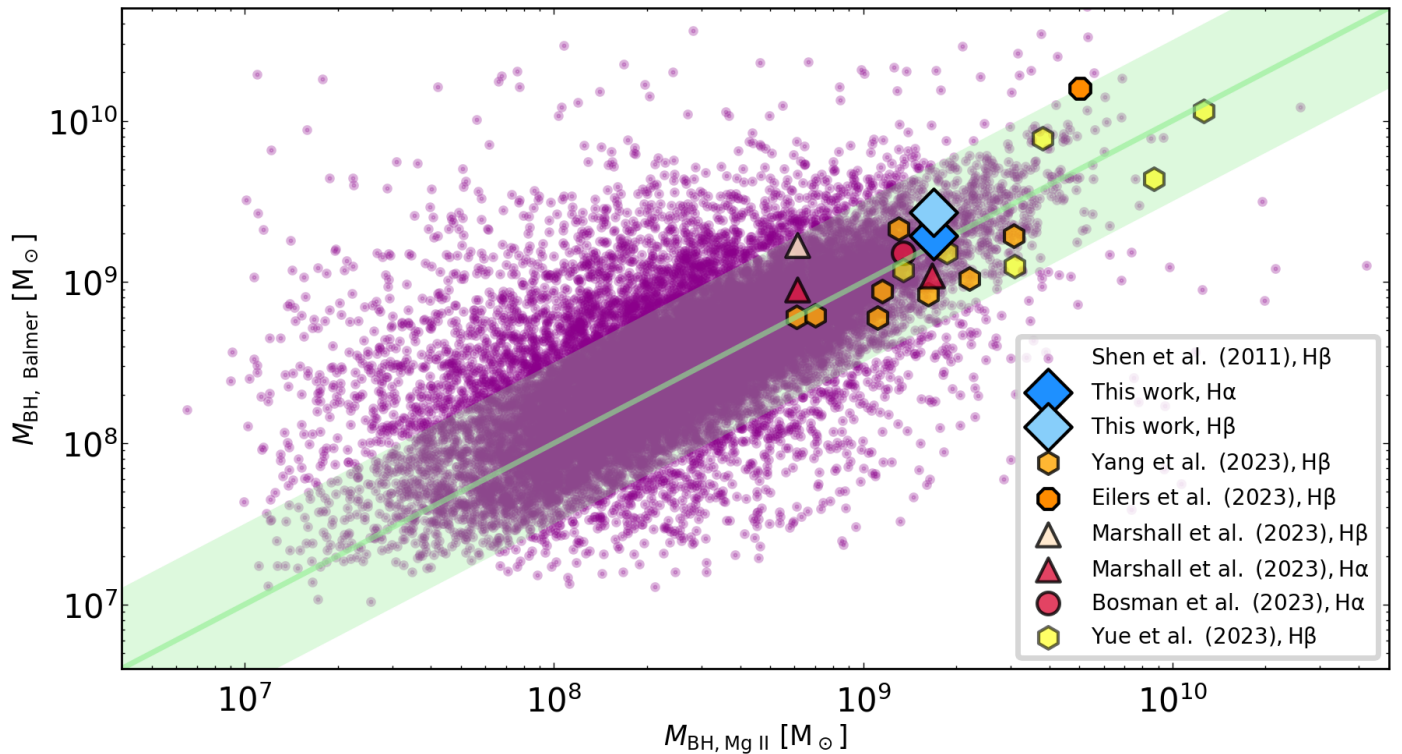$$M_{\rm BH,MgII} = (2.65^{+0.32}_{-0.56}) \times 10^9\,M_\odot$$

Fig. 6. Black hole masses from SDSS (Shen et al. 2011) and $z > 6$ quasars (Bosman et al. 2023; Eilers et al. 2023; Marshall et al. 2023; Yang et al. 2023; Yue et al. 2023), with both Mg II and Balmer line based measurements. The green line shows the one-to-one relation. PJ308-21 is indicated with blue diamonds (JWST/NIRSpec and VLT/XSHOOTER data). Overall, the $z > 6$ quasars show nice agreement between the Mg II and Hβ or Hα-based $M_{\rm BH}$, consistent with the ~ 0.5 dex scatter of the low-redshift estimates (green region; Vestergaard & Peterson 2006). While a larger sample is needed to confirm these results, these first JWST estimates suggest that the Mg II is a reliable tracer of the black hole mass at both low and high-redshift.

This value is consistent with the Hβ estimate. For this quasar Farina et al. (2022) also derived a C IV based black hole mass using the relation of Coatman et al. (2017), i.e., $M_{\rm BH,CIV} = (2.09^{+0.52}_{-0.49}) \times 10^9$ M$_\odot$, which is consistent with the estimates from the other lines.

Figure 6 compares the PJ308-21 black hole mass estimates with estimates from SDSS (Shen et al. 2011) and the other $z > 6$ quasars with both Mg II and Hβ or Hα black hole mass measurements from JWST data (Bosman et al. 2023; Eilers et al. 2023; Marshall et al. 2023; Yang et al. 2023; Yue et al. 2023). The Mg II masses are based on the Vestergaard & Osmer (2009) and Shen et al. (2011) calibration (see Pons et al. 2019; Reed et al. 2019; Shen et al. 2019; Wang et al. 2021; Yang et al. 2021; Farina et al. 2022; Mazzucchelli et al. 2023) while the Hβ and Hα measurements are based on Vestergaard & Peterson (2006) and Greene & Ho (2005). Overall, we see that the $z > 6$ QSOs lie well inside the ~ 0.5 dex scatter of the low-redshift estimates. Despite larger sample are necessary to constrain $z > 6$ black hole masses via Balmer lines targeting also less massive black holes (i.e., $M_{\rm BH} \sim 10^8 M_\odot$), these first findings suggest that the Mg II is a reliable mass tracer in distant quasars.

4.2. Eddington ratio

We use the black hole mass to evaluate the Eddington ratio $\lambda_{\rm Edd} = L_{\rm bol}/L_{\rm Edd}$, i.e., the ratio between the quasar bolometric luminosity $L_{\rm bol}$ and the Eddington luminosity $L_{\rm Edd}$ (see Peterson 1997). Assuming spherical geometry, the latter quantity can be

Table 4. Physical quantities of PJ308-21 derived from line fitting.

PJ308-21	
$L_\lambda(5100 \text{ Å})$	$(4.9^{+0.4}_{-0.2}) \times 10^{42}$ erg s^{-1} Å^{-1}
$L(\text{H}\alpha)$	$(1.84 \pm 0.01) \times 10^{45}$ erg s^{-1}
FWHM(Hβ)	4616^{+63}_{-61} km s^{-1}
FWHM(Hα)	3739 ± 26 km s^{-1}
FWHM([O III])	2776^{+75}_{-74} km s^{-1}
$\Delta v_{\rm H\beta}$	87 ± 15 km s^{-1}
$\Delta v_{\rm H\alpha}$	-149 ± 7 km s^{-1}
$\Delta v_{\rm [O III]}$	-1922 ± 39 km s^{-1}
$M_{\rm BH,H\beta}$	$(2.7 \pm 0.2) \times 10^9$ M$_\odot$
$M_{\rm BH,H\alpha}$	$(1.93 \pm 0.03) \times 10^9$ M$_\odot$
$L_{\rm bol}$	$(2.3^{+0.2}_{-0.1}) \times 10^{47}$ erg s^{-1}
$\lambda_{\rm Edd,H\beta}$	$0.67^{+0.12}_{-0.05}$
$\lambda_{\rm Edd,H\alpha}$	$0.96^{+0.10}_{-0.06}$
$EW_{\rm [O III]}$	19 ± 2 Å
$EW_{\rm H\beta}$	118^{+8}_{-11} Å
$EW_{\rm Fe II}$	43^{+2}_{-3} Å
$R_{\rm Fe II}$	$0.36^{+0.04}_{-0.06}$

Notes. We report the random errors from the MCMC fit. The statistical uncertainty, due to object-to-object differences, on the black hole mass estimates is ~ 0.5 dex (Vestergaard & Peterson 2006) and affects also the Eddington ratios.

written as:

$$L_{\rm Edd} = \frac{4\pi G M_{\rm BH} m_{\rm p} c}{\sigma_{\rm T}} = 1.257 \times 10^{38} \left(\frac{M_{\rm BH}}{M_\odot}\right) \text{erg s}^{-1}$$

where σ_T is the cross-section for Thomson scattering, m_p is the proton mass and c is the light speed in vacuum. Based on the $M_{BH,H\beta}$ estimate, we find for PJ308-21 $L_{Edd,H\beta} = (3.4^{+0.3}_{-0.1}) \times 10^{47}$ erg s^{-1} ($L_{Edd,H\alpha} = (2.43 \pm 0.04) \times 10^{47}$ erg s^{-1}). The bolometric luminosity L_{bol} can be estimated from the monochromatic luminosity $L_\lambda(5100\text{Å})$ by assuming a bolometric correction. We use the relation from Richards et al. (2006), updated by Shen et al. (2011):

$$L_{bol} = 9.26 \times \lambda L_\lambda(5100\text{Å})$$

based on 259 quasars from SDSS. This gives a QSO bolometric luminosity of $L_{bol} = (2.3^{+0.2}_{-0.1}) \times 10^{47}$ erg s^{-1}. Therefore, the Eddington ratio for PJ308-21 based on the Hβ line is $\lambda_{Edd,H\beta} = 0.67^{+0.12}_{-0.05}$ ($\lambda_{Edd,H\alpha} = 0.96^{+0.10}_{-0.06}$ for Hα). We note that adopting a different bolometric correction would imply lower Eddington ratio, in the range $0.32 < \lambda_{Edd,H\beta} < 0.47$ ($0.45 < \lambda_{Edd,H\alpha} < 0.66$ for Hα; Shen et al. 2011; Krawczyk et al. 2013; Saccheo et al. 2023). We note also that the true uncertainty on λ_{Edd} is likely higher due to the statistical uncertainty, due to object-to-object differences, on the black hole mass calibrations and on the bolometric luminosity.

We can look at the high Eddington ratio of PJ308-21 in the context of the $z \sim 6$ QSO population (see also Yang et al. 2023). Based on VLT/XSHOOTER spectra of 38 QSO at $5.8 < z < 7.5$, Farina et al. (2022) found that these objects show higher values of λ_{Edd} than the low-redshift population at fixed L_{bol} (Shen et al. 2011). This suggests that in the early Universe QSOs tended to accrete at higher rates than the low-z AGN, even if exceptions are present among low-luminosity quasars (Kim et al. 2018; Matsuoka et al. 2019). Besides, this trend can be affected by observational biases toward a selection of more massive black holes and higher bolometric luminosities (and thus higher Eddington ratios) at high redshift. PJ308-21 has an Eddington ratio based on Hβ and Hα above, but still consistent (given the statistical uncertainties in the black hole masses) with the median value $\lambda_{Edd}^{med} = 0.48^{+0.06}_{-0.02}$ of the $5.8 < z < 7.5$ quasar sample of Farina et al. (2022). The Hβ value is also in perfect agreement with the Mg II-based $\lambda_{Edd} = 0.66^{+0.17}_{-0.07}$ for PJ308-21 measured by Farina et al. (2022) adopting the bolometric correction for 3000 Å of Richards et al. (2006) updated by Shen et al. (2011).

4.3. Correlations between Fe II, [O III] and Hβ

As initially shown by Boroson & Green (1992), the strength of the Fe II and [O III] $\lambda5007$ emission is anti-correlated in low-redshift quasars. The so-called "Eigenvector 1 correlation" ($EV1$) was then confirmed by other papers (e.g., Sulentic et al. 2004, 2006; Kovačević et al. 2010; Runnoe et al. 2013; Pennell et al. 2017), comparing the Fe II strength, quantified by the ratio between the Fe II and Hβ rest-frame equivalent width, i.e., $R_{Fe\,II} = EW_{Fe\,II}/EW_{H\beta}$, and the [O III] rest-frame equivalent width, $EW_{[O\,III]}$. The physical origin of this relation is still poorly understood, although it may be related to the processes governing the black hole accretion (Shen 2016). At higher redshifts, Shen (2016) found that the anti-correlation is in place in $1.5 < z < 3.5$ QSOs, with slightly lower $EW_{[O\,III]}$ compared to low redshift (see also Sulentic et al. 2004, 2006). Before the JWST launch, it was not possible to investigate this relation for quasars at $z > 6$. First results using slitless JWST/NIRCam spectroscopy in eight $z > 6$ QSOs by Yang et al. (2023) are consistent with low-redshift samples.

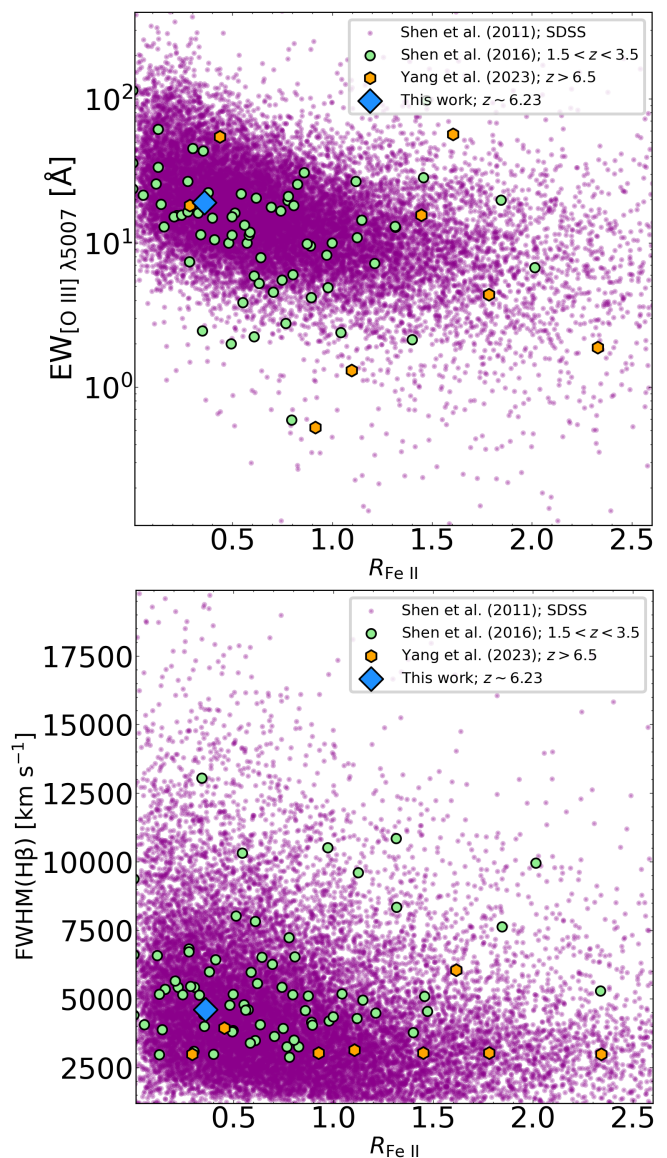For PJ308-21 we find an [O III] $\lambda5007$ rest-frame equivalent

Fig. 7. Anti-correlations between the Fe II strength, parametrized by $R_{Fe\,II}$, the [O III] EW and Hβ FWHM. *Top panel*: the anti-correlation between $R_{Fe\,II}$ and $EW_{[O\,III]}$ (EV1 relation). PJ308-21 (blue diamond) shows a value in agreement with both low-redshift (Shen et al. 2011), $1.5 < z < 3.5$ (Shen 2016) and $z > 6$ quasars (Yang et al. 2023). *Bottom panel*: anti-correlation between $R_{Fe\,II}$ and FWHM(Hβ) (2D EV1). Also in this case, the PJ308-21 value appears consistent with the findings of other studies.

width $EW_{[O\,III]} = 19 \pm 2$ Å. We measure this quantity including both the [O III] $\lambda5007$ narrow and broad component, following Shen et al. (2011). The EW of the Hβ broad component is $EW_{H\beta} = 118^{-8}_{-11}$ Å while the $EW_{Fe\,II}$ is 43^{+2}_{-3} Å. The latter quantity was obtained by directly integrating the continuum-subtracted Fe II emission in the range $4434 - 4684$ Å (Shen et al. 2011). We integrate the data rather than the Fe II line fit in order to avoid uncertainties in the iron modeling (see Sect. 3.2.2 and Fig. 4, bottom panel). The resulting $R_{Fe\,II}$ is $R_{Fe\,II} = 0.36^{+0.04}_{-0.06}$. We note that the iron emission may be contaminated by the blue/red wing of the Hβ/ Hγ BLR lines. We neglect this contribution when estimating the iron EW for consistency with Shen et al. (2011). We also test that subtracting the Hβ and Hγ emis-

sion does not significantly affect any of the results about the EV correlations for the quasar. In that case we obtain indeed $EW_{\text{Fe II}}$ is 36^{+2}_{-3} Å and $R_{\text{Fe II}} = 0.31^{+0.03}_{-0.05}$, which place PJ308-21 in a similar location in the two panels of Figure 7.

In Figure 7 (top panel), we compare PJ308-21 with the DR7 SDSS quasars from Shen et al. (2011) and a sample of 74 luminous ($L_{\text{bol}} = 10^{46.2-48.2}$ erg s^{-1}) $1.5 < z < 3.5$ QSOs (Shen 2016). We show also the eight $z > 6$ quasars from Yang et al. (2023). Our source is consistent with the values presented by both low-redshift and high-redshift quasars, showing a low $R_{\text{Fe II}}$ corresponding to a high $EW_{\text{[O III]}}$.

We also explore the anticorrelation between $R_{\text{Fe II}}$ and the Hβ FWHM ("2D EV1", e.g., Boroson & Green 1992; Shen & Ho 2014); see Figure 7 (bottom panel). Compared to low redshift objects, high-redshift quasars show a systematic offset in the Hβ FWHM up to $z > 6$ (Shen 2016; Yang et al. 2023). This is due to a selection effect as at high redshift we mainly sample the most massive black holes, which correspond to larger Hβ FWHM. We find that, for this relation as well, PJ308-21 shows values in line with the findings for the DR7 SDSS quasars and higher-redshift QSOs.

4.4. Velocity shifts

Several papers have studied the bulk velocity shifts of the BLR gas (e.g., Gaskell 1982; Richards et al. 2002; Meyer et al. 2019; Onoue et al. 2020). In particular, high-ionization lines like C IV λ1549 and Si IV λ1397 have significantly higher velocity shifts relative to low-ionization broad lines, such as Mg II and Balmer lines. These velocity offsets are thought to be due to outflowing clouds from the BLR driven by winds or X-ray radiation (Murray & Chiang 1995).

According to Schindler et al. (2020), PJ308-21 displays a C IV blueshifted emission of -2823^{+200}_{-188} km s^{-1} with respect to the [C II] systemic velocity. On the other hand, the low ionization Mg II line shows a blueshift of -167^{+98}_{-101} km s^{-1}. From the NIRSpec spectrum, we find that the Hα emission is blueshifted of $\Delta v_{\text{H}\alpha} = -149 \pm 7$ km s^{-1} while the Hβ line is redshifted of $\Delta v_{\text{H}\beta} = 87 \pm 15$ km s^{-1}. Shen et al. (2011) found no significant offset in Hα and Hβ relative to the narrow [O III] and [S II] lines in their SDSS DR7 sample of quasars. The overall small shifts found for the Mg II and Balmer lines in PJ308-21 suggest that the clouds these lines originate from are mostly dominated by virial motion around the black hole rather than outflowing material (Gaskell & Goosmann 2013), which is a required assumption for the validity of the single-epoch black hole mass measurements presented in Sect 4.1. We also estimate the velocity shift of the [O III] broad components, which is commonly used as a tracer of ionized outflows (e.g., Cano-Díaz et al. 2012; Harrison et al. 2012, 2014; Carniani et al. 2015; Zakamska et al. 2016; Loiacono et al. 2019; Tozzi et al. 2021). These outflows are often found to extend to kpc-scales, well beyond the nuclear region, and thus can affect the host galaxy and its gas content. As discussed in Sect. 3.2, we fitted the [O III] emission using four Gaussian functions, two narrow and two broad, with the former centered on the systemic velocity of the system (Figure 5, left). The [O III] λ5007 broad line is blueshifted by $\Delta v_{\text{[O III]}} = -1922 \pm 39$ km s^{-1} relative to the systemic velocity traced by [C II]. The FWHM of the same line is FWHM([O III]) $= 2776^{+75}_{-74}$ km s^{-1}. While this suggests significant outflowing ionized gas from the NLR of the quasar (see Figure 8), we highlight that the [O III] modeling in this source is quite challenging, as this emission is strongly blended with the Hβ and iron lines from the BLR.
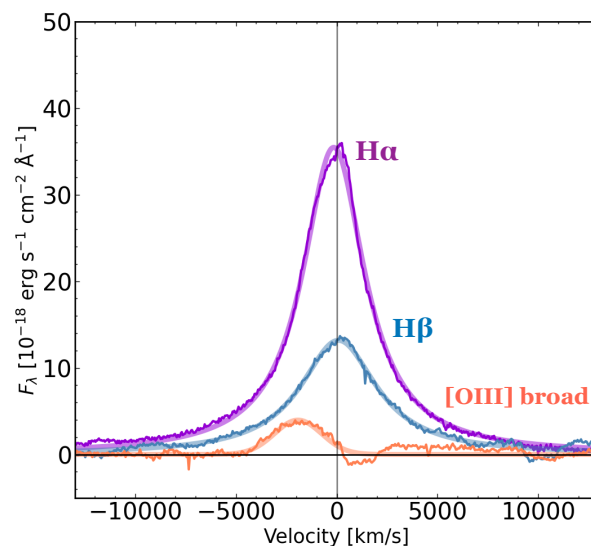

Fig. 8. Emission from the Hα and Hβ BLR lines and the [O III] λ5007 broad component as a function of the velocity. Both the subtracted-data (solid lines) and the fitted models (semi-transparent thick curves) are shown. The systemic velocity, set by the vertical grey line, is based on the [C II] redshift. The Hα and Hβ lines are offset of a small amount compared to the zero-reference point ($\Delta v_{\text{H}\alpha} = -149 \pm 7$ km s^{-1} and $\Delta v_{\text{H}\beta} = 87 \pm 15$ km s^{-1}). On the other hand, we see that the [O III] λ5007 broad component shows a velocity blueshift of $\Delta v_{\text{[O III]}} = -1922 \pm 39$ km s^{-1} and a FWHM([O III]) $= 2776^{+75}_{-74}$ km s^{-1}. This blueshifted emission highlights possible outflowing material from the QSO host galaxy.

This makes the errors on $\Delta v_{\text{[O III]}}$ and FWHM([O III]) likely underestimated. Strong blueshifted [O III] emission was also found in two out of $z > 6.5$ quasars studied by Yang et al. (2023). In their case, the velocity offsets are lower at ~ -630 km s^{-1} and ~ -1690 km s^{-1}, and FWHM~ 1461 km s^{-1} and ~ 3805 km s^{-1}.

High-velocity outflows in high-z sources are predicted by models to play a role in regulating both the black hole and galaxy growth (e.g., Di Matteo et al. 2005; Hopkins et al. 2016; Weinberger et al. 2017; Costa et al. 2022; Lupi et al. 2022). At intermediate and low redshift, several studies using optical/NIR, far-infrared and mm/sub-mm facilities assessed the role of outflows in shaping the AGN host galaxies (e.g., Feruglio et al. 2010; Sturm et al. 2011; Liu et al. 2013; Zakamska & Greene 2014; Brusa et al. 2015b; Cresci et al. 2015; Nardini et al. 2015; Bischetti et al. 2017; Fiore et al. 2017; González-Alfonso et al. 2017). Outflows have been detected in only a small number of $z \sim 6$ quasars (Stanley et al. 2019; Bischetti et al. 2022; Butler et al. 2023; Salak et al. 2024) and in some cases their presence is ambiguous (Maiolino et al. 2012; Cicone et al. 2015; Meyer et al. 2022b). The first JWST results suggest the existence of strong [O III] outflows at $z > 6$ for the first time, demonstrating the capabilities of JWST in detecting these features at the end of Reionization. With the uncertainties in mind, PJ308-21 shows remarkably large velocity offset and FWHM of the [O III] emission, significantly higher than typical values at lower redshift (Liu et al. 2013; Rodríguez Zaurín et al. 2013; Brusa et al. 2015a; Perna et al. 2015; Harrison et al. 2016; Bischetti et al. 2017).

Unfortunately, we cannot estimate the size of the outflowing [O III] component from the IFU data as it is outshone by the QSO emission. This quantity would enable indeed an estimate of the mass outflow rate, i.e., the amount of ionized gas expelled

per time unit (e.g., Cano-Díaz et al. 2012; Carniani et al. 2015). However, after PSF subtraction, Decarli et al. (in prep.) find a possible redshifted component located above the host galaxy, extending to the Northwest with much lower velocity (~ 300 km s^{-1}) which may trace the receding cone of the outflow and can be related to the Lyman α nebula enshrouding the quasar Farina et al. (2022). Farina et al. (in prep.) will discuss this component in greater detail.

5. Conclusions

We presented the JWST/NIRSpec IFU spectrum of the $z \sim 6.23$ quasar PJ308-21. The NIRSpec dataset shows the rest-frame optical emission in the $3700 - 7300$ Å range. We briefly summarize the main results of this paper:

i) We estimate the black hole mass using the Hβ and Hα broad lines. We find that PJ308-21 harbors a mature black hole, with $M_{\mathrm{BH,H\beta}} = (2.7 \pm 0.2) \times 10^9$ M$_\odot$. The Hα-based black hole mass is $M_{\mathrm{BH,H\alpha}} = (1.93 \pm 0.03) \times 10^9$ M$_\odot$. The two values are consistent within a factor $\lesssim 1.5$, within the ~ 0.5 dex statistical uncertainties of the mass calibrations. The Hβ value is also consistent with a previous estimate of the black hole mass $M_{\mathrm{BH,Mg\,II}} = (2.65^{+0.32}_{-0.56}) \times 10^9$ M$_\odot$ derived by Farina et al. (2022) using the Mg II line. All the estimates are consistent with the C IV based black hole mass by Farina et al. (2022).

ii) PJ308-21 shows a high Eddington ratio $\lambda_{\mathrm{Edd,H\beta}} = 0.67^{+0.12}_{-0.05}$ ($\lambda_{\mathrm{Edd,H\alpha}} = 0.96^{+0.10}_{-0.06}$), in line with the population of $z \gtrsim 6$ QSOs (see Farina et al. 2022; Yang et al. 2023).

iii) PJ308-21 shows values of EW$_{\mathrm{[O\,III]}}$ and $R_{\mathrm{Fe\,II}}$ similar to those of low-z (Shen et al. 2011) and intermediate redshift quasars ($1.5 < z < 3.5$, Shen 2016). The same holds for the Hβ FWHM and $R_{\mathrm{Fe\,II}}$ anticorrelation ("2D EV1").

iv) We find evidence of a blueshifted and broad [O III] component, with a velocity shift $\Delta v_{\mathrm{[O\,III]}} = -1922 \pm 39$ km s^{-1} relative to the [C II]-based systemic velocity, and a FWHM([O III]) $= 2776^{+75}_{-74}$ km s^{-1}. Both the FWHM and $\Delta v_{\mathrm{[O\,III]}}$ are larger than in quasars at lower redshift. Despite the uncertainties affecting the line fitting, this could be one of the first detections of an [O III] outflow from a $z \gtrsim 6$ quasar.

Our study demonstrates the unique capabilities of JWST/NIRSpec in dissecting the emission from quasars at $z \gtrsim 6$ with modest amounts of telescope time (~ 1.5 hrs on source in our case). Future NIRSpec campaigns on larger samples will be crucial to unveiling new and unparalleled insights on the quasar population at cosmic dawn.

References

Aravena, M., Decarli, R., Walter, F., et al. 2016, ApJ, 833, 71

Bañados, E., Venemans, B. P., Decarli, R., et al. 2016, ApJS, 227, 11

Bentz, M. C., Walsh, J. L., Barth, A. J., et al. 2009, ApJ, 705, 199

Bischetti, M., Feruglio, C., D'Odorico, V., et al. 2022, Nature, 605, 244

Bischetti, M., Piconcelli, E., Vietri, G., et al. 2017, A&A, 598, A122

Böker, T., Arribas, S., Lützgendorf, N., et al. 2022, A&A, 661, A82

Borisova, E., Cantalupo, S., Lilly, S. J., et al. 2016, ApJ, 831, 39

Boroson, T. A. & Green, R. F. 1992, ApJS, 80, 109

Bosman, S. E. I., Álvarez-Márquez, J., Colina, L., et al. 2023, arXiv e-prints, arXiv:2307.14414

Bouwens, R. J., Illingworth, G. D., Oesch, P. A., et al. 2015, ApJ, 803, 34

Brusa, M., Bongiorno, A., Cresci, G., et al. 2015a, MNRAS, 446, 2394

Brusa, M., Feruglio, C., Cresci, G., et al. 2015b, A&A, 578, A11

Butler, K. M., van der Werf, P. P., Topkaras, T., et al. 2023, ApJ, 944, 134

Calura, F., Gilli, R., Vignali, C., et al. 2014, MNRAS, 438, 2765

Cano-Díaz, M., Maiolino, R., Marconi, A., et al. 2012, A&A, 537, L8

Carniani, S., Marconi, A., Maiolino, R., et al. 2015, A&A, 580, A102

Cicone, C., Maiolino, R., Gallerani, S., et al. 2015, A&A, 574, A14

Coatman, L., Hewett, P. C., Banerji, M., et al. 2017, MNRAS, 465, 2120

Connor, T., Bañados, E., Stern, D., et al. 2019, ApJ, 887, 171

Costa, T., Arrigoni Battaia, F., Farina, E. P., et al. 2022, MNRAS, 517, 1767

Cresci, G., Mainieri, V., Brusa, M., et al. 2015, ApJ, 799, 82

De Rosa, G., Fausnaugh, M. M., Grier, C. J., et al. 2018, ApJ, 866, 133

De Rosa, G., Venemans, B. P., Decarli, R., et al. 2014, ApJ, 790, 145

Decarli, R., Dotti, M., Bañados, E., et al. 2019, ApJ, 880, 157

Decarli, R., Pensabene, A., Diaz-Santos, T., et al. 2023, A&A, 673, A157

Decarli, R., Pensabene, A., Venemans, B., et al. 2022, A&A, 662, A60

Decarli, R., Walter, F., Venemans, B. P., et al. 2017, Nature, 545, 457

Decarli, R., Walter, F., Venemans, B. P., et al. 2018, ApJ, 854, 97

Di Matteo, T., Springel, V., & Hernquist, L. 2005, Nature, 433, 604

Ding, X., Onoue, M., Silverman, J. D., et al. 2023, Nature, 621, 51

Drake, A. B., Farina, E. P., Neeleman, M., et al. 2019, ApJ, 881, 131

Eilers, A.-C., Simcoe, R. A., Yue, M., et al. 2023, ApJ, 950, 68

Fan, X., Bañados, E., & Simcoe, R. A. 2023, ARA&A, 61, 373

Farina, E. P., Arrigoni-Battaia, F., Costa, T., et al. 2019, ApJ, 887, 196

Farina, E. P., Schindler, J.-T., Walter, F., et al. 2022, ApJ, 941, 106

Farina, E. P., Venemans, B. P., Decarli, R., et al. 2017, ApJ, 848, 78

Feruglio, C., Maiolino, R., Piconcelli, E., et al. 2010, A&A, 518, L155

Fiore, F., Feruglio, C., Shankar, F., et al. 2017, A&A, 601, A143

Foreman-Mackey, D., Hogg, D. W., Lang, D., & Goodman, J. 2013, PASP, 125, 306

Gardner, J. P., Mather, J. C., Abbott, R., et al. 2023, PASP, 135, 068001

Gaskell, C. M. 1982, ApJ, 263, 79

Gaskell, C. M. & Goosmann, R. W. 2013, ApJ, 769, 30

González-Alfonso, E., Fischer, J., Spoon, H. W. W., et al. 2017, ApJ, 836, 11

Greene, J. E. & Ho, L. C. 2005, ApJ, 630, 122

Habouzit, M., Volonteri, M., Somerville, R. S., et al. 2019, MNRAS, 489, 1206

Harikane, Y., Ouchi, M., Shibuya, T., et al. 2018, ApJ, 859, 84

Harrison, C. M., Alexander, D. M., Mullaney, J. R., et al. 2016, MNRAS, 456, 1195

Harrison, C. M., Alexander, D. M., Mullaney, J. R., & Swinbank, A. M. 2014, MNRAS, 441, 3306

Harrison, C. M., Alexander, D. M., Swinbank, A. M., et al. 2012, MNRAS, 426, 1073

Homayouni, Y., Trump, J. R., Grier, C. J., et al. 2020, ApJ, 901, 55

Hopkins, P. F., Torrey, P., Faucher-Giguère, C.-A., Quataert, E., & Murray, N. 2016, MNRAS, 458, 816

Inayoshi, K., Visbal, E., & Haiman, Z. 2020, ARA&A, 58, 27

Izumi, T., Onoue, M., Matsuoka, Y., et al. 2019, PASJ, 71, 111

Jakobsen, P., Ferruit, P., Alves de Oliveira, C., et al. 2022, A&A, 661, A80

Jun, H. D., Im, M., Lee, H. M., et al. 2015, ApJ, 806, 109

Kashino, D., Lilly, S. J., Matthee, J., et al. 2023, ApJ, 950, 66

Kaspi, S., Brandt, W. N., Maoz, D., et al. 2021, ApJ, 915, 129

Kaspi, S., Maoz, D., Netzer, H., et al. 2005, ApJ, 629, 61

Kim, Y., Im, M., Jeon, Y., et al. 2018, ApJ, 855, 138

Kollatschny, W. & Zetzl, M. 2013, A&A, 549, A100

Kovačević, J., Popović, L. Č., & Dimitrijević, M. S. 2010, ApJS, 189, 15

Krawczyk, C. M., Richards, G. T., Mehta, S. S., et al. 2013, ApJS, 206, 4

Kurk, J. D., Walter, F., Fan, X., et al. 2007, ApJ, 669, 32

Li, J., Wang, R., Cox, P., et al. 2020, ApJ, 900, 131

Lira, P., Kaspi, S., Netzer, H., et al. 2018, ApJ, 865, 56

Liu, G., Zakamska, N. L., Greene, J. E., Nesvadba, N. P. H., & Liu, X. 2013, MNRAS, 436, 2576

Loiacono, F., Talia, M., Fraternali, F., et al. 2019, MNRAS, 489, 681

Lupi, A., Volonteri, M., Decarli, R., Bovino, S., & Silk, J. 2022, MNRAS, 510, 5760

Maiolino, R., Gallerani, S., Neri, R., et al. 2012, MNRAS, 425, L66

Marshall, M. A., Perna, M., Willott, C. J., et al. 2023, arXiv e-prints, arXiv:2302.04795

Marziani, P., del Olmo, A., Martínez-Carballo, M. A., et al. 2019, A&A, 627, A88

Matsuoka, Y., Onoue, M., Kashikawa, N., et al. 2019, ApJ, 872, L2

Mazzucchelli, C., Bañados, E., Decarli, R., et al. 2017a, ApJ, 834, 83

Mazzucchelli, C., Bañados, E., Venemans, B. P., et al. 2017b, ApJ, 849, 91

Mazzucchelli, C., Bischetti, M., D'Odorico, V., et al. 2023, A&A, 676, A71

Meyer, R. A., Bosman, S. E. I., & Ellis, R. S. 2019, MNRAS, 487, 3305

Meyer, R. A., Decarli, R., Walter, F., et al. 2022a, ApJ, 927, 141

Meyer, R. A., Walter, F., Cicone, C., et al. 2022b, ApJ, 927, 152

Murray, N. & Chiang, J. 1995, ApJ, 454, L105

Nardini, E., Reeves, J. N., Gofford, J., et al. 2015, Science, 347, 860

Neeleman, M., Bañados, E., Walter, F., et al. 2019, ApJ, 882, 10

Neeleman, M., Novak, M., Venemans, B. P., et al. 2021, ApJ, 911, 141

Novak, M., Bañados, E., Decarli, R., et al. 2019, ApJ, 881, 63

Onoue, M., Bañados, E., Mazzucchelli, C., et al. 2020, ApJ, 898, 105

Onoue, M., Kashikawa, N., Matsuoka, Y., et al. 2019, ApJ, 880, 77

Osterbrock, D. E. & Ferland, G. J. 2006, Astrophysics of gaseous nebulae and active galactic nuclei

Ota, K., Iye, M., Kashikawa, N., et al. 2017, ApJ, 844, 85

Pennell, A., Runnoe, J. C., & Brotherton, M. S. 2017, MNRAS, 468, 1433

Pensabene, A., Carniani, S., Perna, M., et al. 2020, A&A, 637, A84

Pensabene, A., Decarli, R., Bañados, E., et al. 2021, A&A, 652, A66

Perna, M., Arribas, S., Marshall, M., et al. 2023, arXiv e-prints, arXiv:2304.06756

Perna, M., Brusa, M., Cresci, G., et al. 2015, A&A, 574, A82

Peterson, B. M. 1997, An Introduction to Active Galactic Nuclei

Pons, E., McMahon, R. G., Simcoe, R. A., et al. 2019, MNRAS, 484, 5142

Rauscher, B. J. 2023, arXiv e-prints, arXiv:2306.03250

Reed, S. L., Banerji, M., Becker, G. D., et al. 2019, MNRAS, 487, 1874

Richards, G. T., Lacy, M., Storrie-Lombardi, L. J., et al. 2006, ApJS, 166, 470

Richards, G. T., Vanden Berk, D. E., Reichard, T. A., et al. 2002, AJ, 124, 1

Rigby, J. R., Lightsey, P. A., García Marín, M., et al. 2022, arXiv e-prints, arXiv:2211.09890

Rodríguez Zaurín, J., Tadhunter, C. N., Rose, M., & Holt, J. 2013, MNRAS, 432, 138

Runnoe, J. C., Ganguly, R., Brotherton, M. S., & DiPompeo, M. A. 2013, MNRAS, 433, 1778

Saccheo, I., Bongiorno, A., Piconcelli, E., et al. 2023, A&A, 671, A34

Salak, D., Hashimoto, T., Inoue, A. K., et al. 2024, ApJ, 962, 1

Salmon, B., Papovich, C., Finkelstein, S. L., et al. 2015, ApJ, 799, 183

Schindler, J.-T., Farina, E. P., Bañados, E., et al. 2020, ApJ, 905, 51

Shao, Y., Wang, R., Weiss, A., et al. 2022, A&A, 668, A121

Shapovalova, A. I., Popović, L. Č., Burenkov, A. N., et al. 2012, ApJS, 202, 10

Shen, Y. 2013, Bulletin of the Astronomical Society of India, 41, 61

Shen, Y. 2016, ApJ, 817, 55

Shen, Y. & Ho, L. C. 2014, Nature, 513, 210

Shen, Y., Richards, G. T., Strauss, M. A., et al. 2011, ApJS, 194, 45

Shen, Y., Wu, J., Jiang, L., et al. 2019, ApJ, 873, 35

Stanley, F., Jolly, J. B., König, S., & Knudsen, K. K. 2019, A&A, 631, A78

Sturm, E., González-Alfonso, E., Veilleux, S., et al. 2011, ApJ, 733, L16

Sulentic, J. W., Repetto, P., Stirpe, G. M., et al. 2006, A&A, 456, 929

Sulentic, J. W., Stirpe, G. M., Marziani, P., et al. 2004, A&A, 423, 121

Tozzi, G., Cresci, G., Marasco, A., et al. 2021, A&A, 648, A99

Tozzi, G., Maiolino, R., Cresci, G., et al. 2023, MNRAS, 521, 1264

Tripodi, R., Feruglio, C., Fiore, F., et al. 2022, A&A, 665, A107

Vanden Berk, D. E., Richards, G. T., Bauer, A., et al. 2001, AJ, 122, 549

Vanzella, E., Fontana, A., Zitrin, A., et al. 2014, ApJ, 783, L12

Venemans, B. P., Decarli, R., Walter, F., et al. 2018, ApJ, 866, 159

Venemans, B. P., Walter, F., Decarli, R., et al. 2017, ApJ, 851, L8

Venemans, B. P., Walter, F., Zschaechner, L., et al. 2016, ApJ, 816, 37

Vestergaard, M. & Osmer, P. S. 2009, ApJ, 699, 800

Vestergaard, M. & Peterson, B. M. 2006, ApJ, 641, 689

Vietri, G., Piconcelli, E., Bischetti, M., et al. 2018, A&A, 617, A81

Volonteri, M., Habouzit, M., & Colpi, M. 2021, Nature Reviews Physics, 3, 732

Walter, F., Bertoldi, F., Carilli, C., et al. 2003, Nature, 424, 406

Walter, F., Neeleman, M., Decarli, R., et al. 2022, ApJ, 927, 21

Walter, F., Riechers, D., Novak, M., et al. 2018, ApJ, 869, L22

Wang, F., Yang, J., Fan, X., et al. 2021, ApJ, 907, L1

Wang, F., Yang, J., Hennawi, J. F., et al. 2023, ApJ, 951, L4

Wang, R., Wagg, J., Carilli, C. L., et al. 2008, AJ, 135, 1201

Weinberger, R., Springel, V., Hernquist, L., et al. 2017, MNRAS, 465, 3291

Willott, C. J., Albert, L., Arzoumanian, D., et al. 2010, AJ, 140, 546

Willott, C. J., Bergeron, J., & Omont, A. 2015, ApJ, 801, 123

Willott, C. J., Bergeron, J., & Omont, A. 2017, ApJ, 850, 108

Willott, C. J., Omont, A., & Bergeron, J. 2013, ApJ, 770, 13

Yang, J., Wang, F., Fan, X., et al. 2021, ApJ, 923, 262

Yang, J., Wang, F., Fan, X., et al. 2023, arXiv e-prints, arXiv:2304.09888

Yue, M., Eilers, A.-C., Simcoe, R. A., et al. 2023, arXiv e-prints, arXiv:2309.04614

Zakamska, N. L. & Greene, J. E. 2014, MNRAS, 442, 784

Zakamska, N. L., Hamann, F., Pâris, I., et al. 2016, MNRAS, 459, 3144

Zana, T., Carniani, S., Prelogović, D., et al. 2023, arXiv e-prints, arXiv:2309.03940

Zuo, W., Wu, X.-B., Fan, X., et al. 2020, ApJ, 896, 40

[1] INAF – Osservatorio di Astrofisica e Scienza dello Spazio di Bologna, via Gobetti 93/3, I-40129, Bologna, Italy. e-mail: `federica.loiacono1@inaf.it`
[2] Gemini Observatory, NSF's NOIRLab, 670 N A'ohoku Place, Hilo, Hawai'i 96720, USA
[3] Max Planck Institut für Astronomie, Königstuhl 17, D-69117, Heidelberg, Germany
[4] Institute for Theoretical Physics, University of Heidelberg, Philosophenweg 16, 69120 Heidelberg, Germany
[5] MIT Kavli Institute for Astrophysics and Space Research, 77 Massachusetts Ave., Cambridge, MA 02139, USA
[6] Hamburger Sternwarte, Universität Hamburg, Gojenbergsweg 112, D-21029 Hamburg, Germany
[7] Department of Astrophysical Sciences, Princeton University, Princeton, NJ 08544 USA
[8] The Niels Bohr Institute, University of Copenhagen, Denmark
[9] Steward Observatory, University of Arizona, 933 N Cherry Avenue, Tucson, AZ 85721, US
[10] Department of Physics, University of Florida, Gainesville, FL 32611-8440, USA
[11] National Radio Astronomy Observatory, P.O. Box O, Socorro, NM 87801, USA
[12] Center for Astrophysics | Harvard & Smithsonian, 60 Garden St., Cambridge, MA 02138, USA
[13] Jet Propulsion Laboratory, California Institute of Technology, 4800 Oak Grove Drive, Pasadena, CA 91109, USA
[14] Max-Planck-Institut für Astrophysik, Karl-Schwarzschild-Straße 1, D-85748 Garching b. München, Germany
[15] Dipartimento di Fisica "G. Occhialini", Università degli Studi di Milano-Bicocca, Piazza della Scienza 3, I-20126 Milano, Italy
[16] INFN, Sezione di Milano-Bicocca, Piazza della Scienza 3, I-20126 Milano, Italy
[17] INAF - Osservatorio Astronomico di Brera, via Brera 20, I-20121 Milano, Italy
[18] Department of Physics, Northwestern College, 101 7th St SW, Orange City, IA 51041
[19] National Research Council of Canada, Herzberg Astronomy & Astrophysics Research Centre, 5071 West Saanich Road, Victoria, BC V9E 2E7, Canada
[20] ARC Centre of Excellence for All Sky Astrophysics in 3 Dimensions (ASTRO 3D), Australia
[21] Instituto de Estudios Astrofísicos, Facultad de Ingeniería y Ciencias, Universidad Diego Portales, Avenida Ejercito Libertador 441, Santiago, Chile
[22] Department of Astronomy, University of Geneva, Chemin Pegasi 51, 1290 Versoix, Switzerland
[23] National Radio Astronomy Observatory, 520 Edgemont Road, Charlottesville, VA, 22903, USA
[24] Leiden Observatory, Leiden University, Niels Bohrweg 2, NL-2333 CA Leiden, Netherlands
[25] I. Physikalisches Institut, Universität zu Köln, Zülpicher Strasse 77, 50937 Köln, Germany
[26] School of Physics and Astronomy, Tel Aviv University, Tel Aviv 69978, Israel
[27] Kapteyn Astronomical Institute, University of Groningen, P.O. Box 800, 9700 AV Groningen, The Netherlands
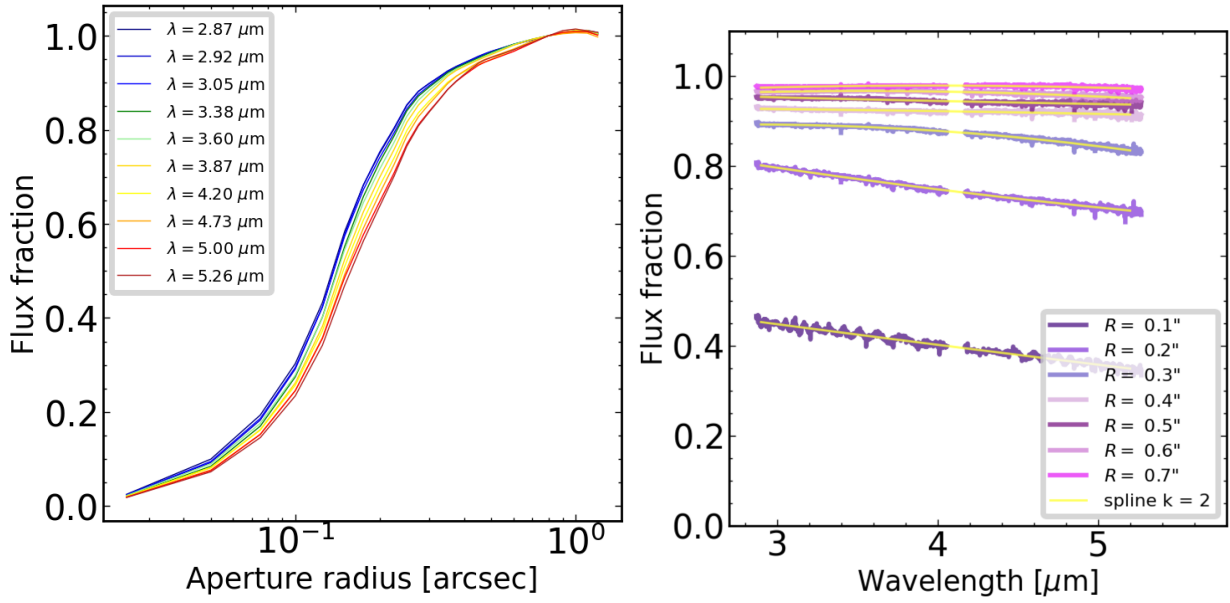
Appendix A: Aperture correction

Fig. A.1. *Left panel*: flux fraction as a function of the aperture radius (NIRSpec/IFU, G395H/F290LP), i.e., the cumulative PSF. Note that the PSF width increases going from blue to red wavelengths. The differences are larger for small radii, as the PSF profile is steeper. The curves are based on observations of the G–dwarf GSPC P330-E used for a Cycle 1 calibration program (ID: 1538). *Right panel*: Flux fractions for apertures with radii $R = 0.1'' - 0.7''$ as a function of the observed wavelength (NIRSpec/IFU, G395H/F290LP). The second-order spline fitted to the data is shown in yellow. The flux fraction decreases with increasing wavelength, especially at small radii.